Acta Biomaterialia 36 (2016) 296–309

Contents lists available at ScienceDirect

Acta Biomaterialia

journal homepage: www.elsevier.com/locate/actabiomat

Full length article

Long-term osseointegration of 3D printed CoCr constructs with an interconnected open-pore architecture prepared by electron beam melting

Furqan A. Shah [a,b,*], Omar Omar [a,b], Felicia Suska [a,b], Anders Snis [b,c], Aleksandar Matic [d], Lena Emanuelsson [a,b], Birgitta Norlindh [a,b], Jukka Lausmaa [b,e], Peter Thomsen [a,b], Anders Palmquist [a,b]

[a] Department of Biomaterials, Sahlgrenska Academy at University of Gothenburg, Göteborg, Sweden
[b] BIOMATCELL VINN Excellence Center of Biomaterials and Cell Therapy, Göteborg, Sweden
[c] Arcam AB, Mölndal, Sweden
[d] Department of Applied Physics, Chalmers University of Technology, Göteborg, Sweden
[e] Department of Chemistry, Materials and Surfaces, SP Technical Research Institute of Sweden, Borås, Sweden

ARTICLE INFO

Article history:
Received 1 December 2015
Received in revised form 11 March 2016
Accepted 17 March 2016
Available online 18 March 2016

Keywords:
3D printing
Additive manufacturing
Electron beam melting
Osseointegration
Alloy
Cobalt chromium
Titanium

ABSTRACT

In orthopaedic surgery, cobalt chromium (CoCr) based alloys are used extensively for their high strength and wear properties, but with concerns over stress shielding and bone resorption due to the high stiffness of CoCr. The structural stiffness, principally related to the bulk and the elastic modulus of the material, may be lowered by appropriate design modifications, to reduce the stiffness mismatch between metal/alloy implants and the adjacent bone. Here, 3D printed CoCr and Ti6Al4V implants of similar macro-geometry and interconnected open-pore architecture prepared by electron beam melting (EBM) were evaluated following 26 week implantation in adult sheep femora. Despite higher total bone-implant contact for Ti6Al4V (39 ± 4%) than CoCr (27 ± 4%), bone formation patterns were similar, e.g., densification around the implant, and gradual ingrowth into the porous network, with more bone in the outer half (periphery) than the inner half (centre). Raman spectroscopy revealed no major differences in mineral crystallinity, the apatite-to-collagen ratio, or the carbonate-to-phosphate ratio. Energy dispersive X-ray spectroscopy showed similar Ca/P ratio of the interfacial tissue adjacent to both materials. Osteocytes made direct contact with CoCr and Ti6Al4V. While osteocyte density and distribution in the new-formed bone were largely similar for the two alloys, higher osteocyte density was observed at the periphery of the porous network for CoCr, attributable to slower remodelling and a different biomechanical environment. The results demonstrate the possibility to achieve bone ingrowth into open-pore CoCr constructs, and attest to the potential for fabricating customised osseointegrated CoCr implants for load-bearing applications.

Statement of Significance

Although cobalt chromium (CoCr) based alloys are used extensively in orthopaedic surgery, stress shielding due to the high stiffness of CoCr is of concern. To reduce the stiffness mismatch between CoCr and bone, CoCr and Ti6Al4V implants having an interconnected open-pore architecture were prepared by electron beam melting (EBM). After six months of submerged healing in sheep, both alloys showed similar patterns of bone formation, with densification around the implant and gradual ingrowth into the porous network. The molecular and elemental composition of the interfacial tissue was similar for both alloys. Osteocytes made direct contact with both alloys, with similar overall osteocyte density and distribution. The work attests to the potential for achieving osseointegration of EBM manufactured porous CoCr implants.

* Corresponding author at: Department of Biomaterials, Sahlgrenska Academy at University of Gothenburg, Göteborg, Sweden.
E-mail address: furqan.ali.shah@biomaterials.gu.se (F.A. Shah).

http://dx.doi.org/10.1016/j.actbio.2016.03.033
1742-7061/

1. Introduction

Cobalt chromium (CoCr) based alloys are extensively used in orthopaedic reconstructive surgery for their high strength and wear properties [1–3]. Uncemented, CoCr femoral stems, with a sintered porous surface have shown promising clinical results [4], allowing bone ingrowth into the porous coated surface [5]. However, periprosthetic bone loss around femoral stems is a problem, even with Ti6Al4V alloys, which otherwise have an outstanding clinical record. And while limited postoperative weight-bearing and aseptic loosening contribute to bone loss [6], bone resorption as a direct consequence of stress shielding due to the high stiffness of CoCr has been reported [7]. The extent of stress shielding experienced by bone around a bone-anchored device depends on the interfacial bonding characteristics, e.g., whether it is cemented or uncemented, the presence of a coating, and the possibility for bone ingrowth [8]. Furthermore, stress shielding is also dependent on the structural stiffness, which is principally related to the bulk and the elastic modulus of the material [8]. Indeed, the overall stiffness of a metal implant and the stress shielding experienced by bone may be reduced by appropriate design modifications.

Additive manufacturing is an emerging fabrication technique, with the potential to overcome the challenges faced in traditional machining. Structures are built up by melting successive thin layers of powder. Material is added, rather than being removed, and complex innovative designs can be produced in an intentional, controlled, and pre-determined manner. Medical implants with an integrated open-pore architecture could be readily produced from a computer-aided design (CAD), enabling either mass production of well-defined implants or customised implants based on patient-specific X-ray imaging [9]. Electron beam melting (EBM) is one of the most promising additive manufacturing techniques for load bearing metal implants [10], allowing modulation of the overall stiffness of the porous structure using both cobalt and titanium based alloys [11].

Osseointegration and biomechanical fixation of CoCr are often considered inferior to titanium (typically Ti6Al4V) alloys [12,13]. Therefore, attempts have been made to improve the biological response to CoCr implants by the use of different coating procedures [14,15]. Interestingly, no differences have been demonstrated between uncoated, solid Ti6Al4V and CoCr implants on the histological [16] and the ultrastructural [17] levels. Furthermore, recent findings have revealed that osseointegration occurs without adverse tissue reactions for EBM-manufactured, solid, CoCr implants [18]. Nevertheless, bone ingrowth into porous CoCr constructs has not yet been evaluated, and little is known about the precise biological and tissue response to such materials.

Bone ingrowth into porous Ti6Al4V implants prepared by EBM [19,20] has been demonstrated previously. The current work aims to evaluate: (i) whether porous CoCr exhibits properties compatible with long-term bone ingrowth similar to Ti6Al4V, and (ii) if there are site-specific differences in bone formation, composition and ultrastructure, depending on the location within and outside the porous network.

2. Materials and methods

2.1. Powder materials, implant fabrication, and surface characterisation

For the Ti6Al4V implants, a plasma-atomised Ti6Al4V ELI powder (Grade 23; ASTM F136 standard) of particle size < 100 μm was used (Fig. 1a). For the CoCr implants, a low carbon gas-atomised CoCr powder (ASTM F75 standard) of particle size < 100 μm was used (Fig. 1b). The chemical compositions of the alloy powders were within the limits of the relevant ASTM standards for medical grade implants (Table 1).

The Ti6Al4V implants were built first, in a single build cycle, followed by the CoCr implants in a separate build cycle in an Arcam EBM A1 system (Arcam AB, Mölndal, Sweden). The upper part of each implant consisted of a solid top whereas the lower part consisted of an interconnected, cylindrical, porous network having a diamond-shaped lattice structure (Fig. 1c, d). Using standard Arcam process parameters for preheating and bulk melting of Ti6Al4V and CoCr, respectively, the implants were built in the z-direction of the cylindrical coordinates with the porous part built on top of the solid part using the same 3D CAD drawing for both materials. The average build temperatures were approximately 680 °C for Ti6Al4V and 780 °C for CoCr, respectively. The melting of CoCr contours and net structures was carried out with the same beam current as for Ti6Al4V, while the beam speed and the contour offset of the 2D polygons were optimised so that the CoCr parts were fully melted and displayed similar dimensions as the Ti6Al4V implants.

All implants were blasted with the same powder as they were built of and machined in the x-y plane to obtain a 2 mm height of the solid top. A shallow notch was machined in the top surface in order to facilitate implant placement. All implants were ultrasonically cleaned in ethanol and visually inspected to ensure that any loose particles and flakes had been removed. After inspection, the implants were cleaned in Extran MA01® (Merck Millipore, Darmstadt, Germany) prior to sterile packaging and subsequent autoclaving.

The macroscopic design and the macro porosity of the implants were evaluated by X-ray micro computed tomography (micro-CT). Three implants of each type were scanned in a (Skyscan 1172, Bruker micro-CT, Kontich, Belgium) operating at 100 kV energy with an Al/Cu filter, for a complete 360° rotation at a step size of 0.7° with an averaging of 5 frames and an image pixel size of 11.88 μm. Reconstruction, analysis, and visualisation were performed using associated Skyscan software. Analysis of porosity and structural dimensions of the porous network was performed for a defined volume of interest confining the porous network only.

The surface chemical composition of the Ti6Al4V and CoCr implants was analysed by X-ray photoelectron spectroscopy (XPS, AXIS Ultra DLD, Kratos Analytical, Manchester, UK) equipped with a monochromatic Al X-ray source. Two implants of each type were analysed. Survey scans were performed for analysis of the atomic composition of the surface, while detailed high-resolution scans were performed to evaluate the oxidation states of specific elements.

The surface morphology was evaluated by scanning electron microscopy (SEM; Leo Ultra 55 FEG SEM, Leo Electron Microscopy Ltd, UK) in the secondary electron mode, operated at 5 kV accelerating voltage. Two implants of each type were evaluated at 100–100,000× magnifications.

2.2. Animal surgery

The animal surgery was conducted in accordance with the provisions of the OECD, EU and US FDA Good Laboratory Practice (GLP) regulations. No deviations from the protocol, standard operating procedures or GLP regulations were considered to significantly affect the outcome. A total of five sheep were operated and each received test and control implants bilaterally in the distal femora (n = 10).

Prior to the surgery, the sheep were fasted 24 h for food and 12 h for water. Each sheep received pre-operative analgesia with buprenorphine (Buprecare®, Axience SAS) and flunixine (Meflosyl® Injectable, Fort Dodge, France). At the time of surgery, anaesthesia

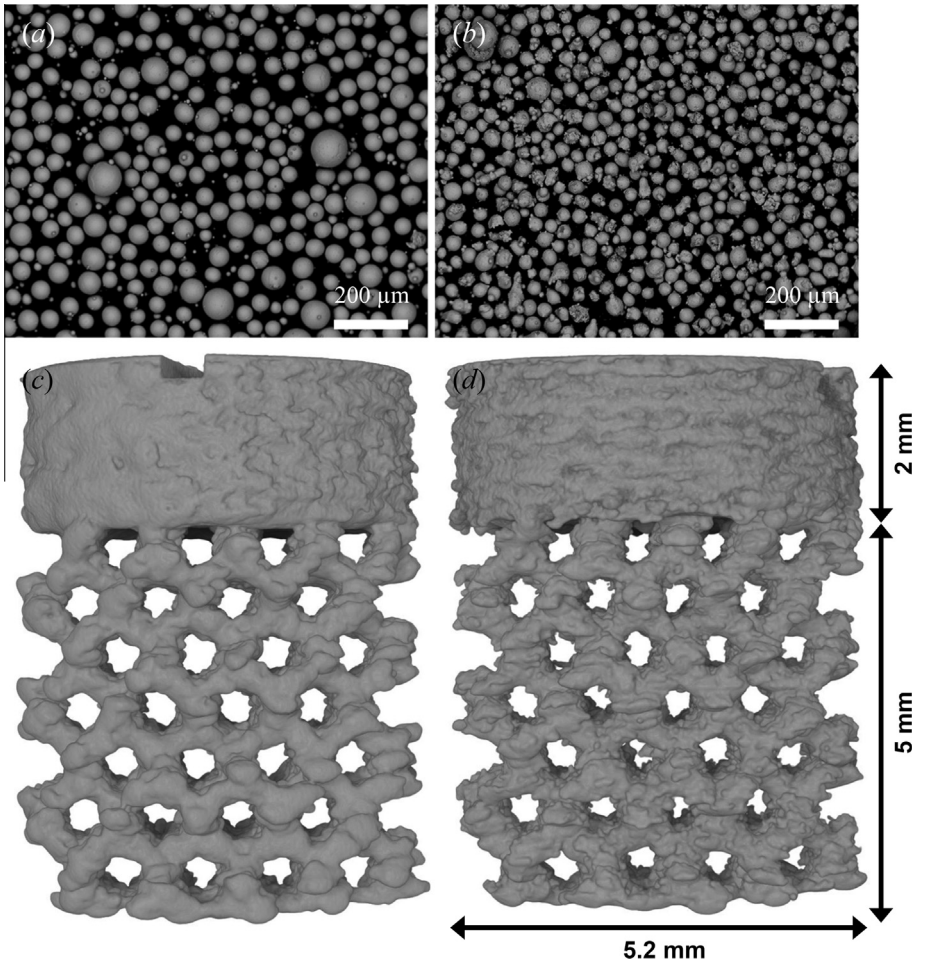

Fig. 1. (a) Ti6Al4V and (b) CoCr starting powders (scanning electron microscopy). 3D rendering of the micro-CT data sets showing the macro-geometry and surface structure of the (c) Ti6Al4V and (d) CoCr implants.

Table 1
Chemical composition of the starting powder (wt.%) and corresponding ASTM standards for Ti6Al4V ELI and CoCr alloy.

	Ti6Al4V		CoCr	
	Current (wt.%)	ASTM F136	Current (wt.%)	ASTM F75
Carbon (C)	0.01	0.08	0.01	<0.35
Nitrogen (N)	0.01	0.05	0.028	<0.25
Oxygen (O)	0.056	0.13	0.065	–
Titanium (Ti)	Bal.	Bal.	0.01	–
Aluminium (Al)	6.32	5.5–6.5	–	–
Vanadium (V)	3.9	3.5-4.5	–	–
Cobalt (Co)	–	–	Bal.	Bal.
Chromium (Cr)	–	–	28.2	27–30
Molybdenum (Mo)	0.01	–	5.6	5–7
Phosphorous (P)	–	–	0.06	–
Silicon (Si)	–	–	0.44	<1.0
Sulphur (S)	–	–	0.004	–
Iron (Fe)	–	0.25	–	–
Tungsten (W)	–	–	0.01	–
Nickel (Ni)	–	–	0.065	<0.5
Manganese (Mn)	<0.01	–	0.63	<1.0

was induced by intravenous administration of a mixture of thiopental (Nesdonal®, Merial, France), pentobarbital (sodium pentobarbital, CEVA Santé animale, France), and atropine (Atropinum sulfuricum, Aguettant, France) followed by inhalation of an O_2-isoflurane (IsoFlo®, Axience SAS) for continued general anaesthesia. The surgical areas were clipped free of fur, scrubbed with povidone iodine (Vetedine® savon, Vetoquinol), wiped with 70% isopropyl alcohol, painted with povidone iodine solution (Vetedine® solution, Vetoquinol) and draped. A perioperative antibiotic, amoxicillin (Duphamox LA®, Pfizer), was administered intramuscularly. A cutaneous incision was made on the medial side of each distal femoral epiphysis, the muscles were separated using blunt dissection, and the periosteum was carefully removed to expose the implantation sites. Drilling and sequential enlargement

of the drill hole were conducted using orthopaedic drills (2, 3 and 5 mm diameters) with a flexible stop, under copious saline irrigation, to create a hole with the final dimensions of 5 mm diameter and 7 mm depth. Each animal received a total of four implants. In each distal femoral epiphysis, either two Ti6Al4V or two CoCr implants were placed 6–12 mm apart, designated as proximal and distal sites. The test (CoCr) and control (Ti6Al4V) implants were randomised between the right or left femur. Using absorbable sutures, the muscles were sutured (PDS II, Ethicon) followed by the subcutaneous layer (Vicryl® 2-0, Ethicon). The skin layer was closed using surgical staples (Appose™ ULC Auto Suture™, Covidien). The wounds were disinfected using an iodine solution (Vetedine®, Vetoquinol) and oxytetracycline (Oxytetrin® spray, Intervet). Postoperatively, buprenorphine was administrated on the night of surgery and for two days after, flunixine was administered daily for five days, and amoxicillin was administered every two days for eight days.

After 26 weeks, the sheep were euthanised by intravenous overdose of pentobarbital (Dolethal®, Vetoquinol). The distal femora were harvested with surrounding tissues, en bloc, and fixed in 10% neutral buffered formalin.

2.3. Histology and histomorphometry

The bone-implant specimens were embedded in plastic resin (LR White, London Resin Co. Ltd, UK) by stepwise dehydration, resin infiltration and polymerisation. The embedded blocks were bisected by sawing and grinding (EXAKT® Apparatebau GmbH & Co, Norderstedt, Germany) [21]. One half-block of each specimen was used to prepare a central ground section (15–20 μm thick), which was stained with toluidine blue. Qualitative histology and quantitative histomorphometry were performed using optical microscopy (Nikon Eclipse E600; Nikon NIS-Elements software).

To determine bone formation inside and around the porous network, a detailed analysis was performed at different locations designated as: (a) centre of the porous network: the inner 1/3rd of the implant, (b) periphery of the porous network: outer 2/3rd of the implant, (c) close to the implant: 0–500 μm from the outer border, (d) distant from the implant: 500–1000 μm from the outer border (Fig. 2), The bone-implant contact (BIC) and bone area (BA) were quantified at the different zones within and outside the porous network.

2.4. Interfacial tissue composition

Selected implant-tissue blocks were polished using 400–2400 grit silicon carbide paper and used for backscattered electron (BSE) SEM imaging in a Quanta 200 environmental SEM (FEI Company, The Netherlands), operated at 20 kV accelerating voltage and 0.5 Torr water vapour pressure. Areas of direct bone-implant contact were selected for Raman spectroscopy and energy dispersive X-ray spectroscopy (EDX).

Raman spectroscopy was used to investigate the composition of the interfacial tissue at the centre and periphery of the porous network, and the new bone formed around the implant. Spectra were collected at room temperature by a nitrogen cooled charge-coupled device (CCD) detector connected to a Dilor XY 800 spectrometer (Horiba, Jobin Yvon GmbH), equipped with a 676 nm Ar/Kr laser operated at ~100 mW, with a 100× objective, 600 groove/mm grating, 300 mm focal length and pinhole size of 100 μm. One sample-pair (from the same animal) was used. Five different locations along the implant surface were analysed in areas of direct bone-implant contact, approximately 5–10 μm from the implant surface at both the centre and the periphery of the porous network. Five locations were also analysed in the new bone formed outside (close and distant regions) the implant, approximately 300–700 μm from the implant surface.

At each position, ten acquisitions were made with an integration time of 20 s each. Raw spectra were truncated between 300 and 1800 cm^{-1} and background fluorescence subtraction was performed by fitting a sixth order polynomial function using the Background Correction program [22] for MATLAB R2013b (Mathworks Inc., Natick, MA). The wavenumber axis was adjusted so that the ν_1 PO_4^{3-} peaks in all spectra corresponded to ~959 cm^{-1}. The baseline-corrected spectra were then normalised using Plot (http://plot.micw.eu/) to show equal intensities of the ν_1 PO_4^{3-} band in all spectra. Curve fitting, using mixed Gaussian and Lorentzian functions, and quantification of integral areas was done using MagicPlot (www.magicplot.com). The Raman metrics investigated included mineral crystallinity, taken as the reciprocal of the full-width at half-maximum (1/FWHM) of the ν_1 PO_4^{3-} peak [23], the apatite-to-collagen ratio, also referred to as the mineral-to-matrix ratio (ν_2 PO_4^{3-}/Amide III [24,25]), and the carbonate-to-phosphate ratio (ν_1 CO_3^{2-}/ν_2 PO_4^{3-} [26]). The integral areas were: ν_1 PO_4^{3-} (~930–980 cm^{-1}), ν_2 PO_4^{3-} (~410–460 cm^{-1}), Amide I (~1620–1700 cm^{-1}), Amide III (~1215–1300 cm^{-1}), and ν_1 CO_3^{2-} (~1050–1100 cm^{-1}) [27].

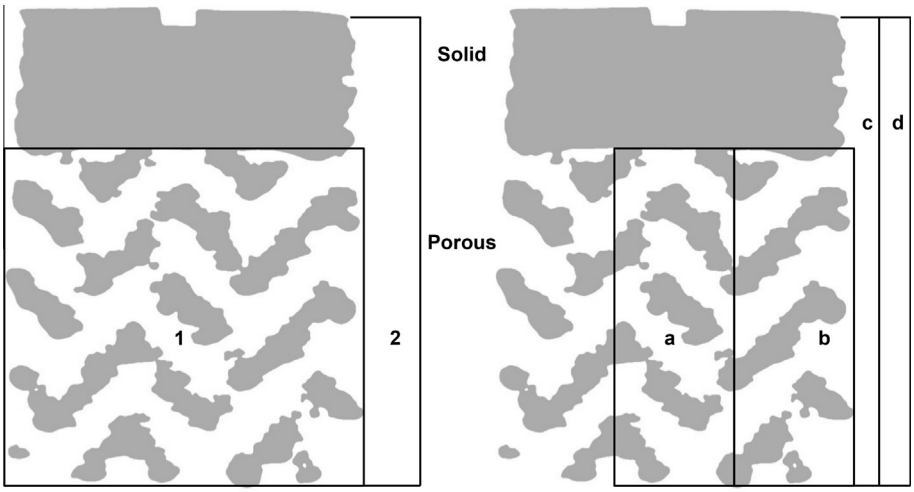

Fig. 2. Illustration of the different locations for quantitative histomorphometry: (1) inside the porous network and (2) outside the implant. The regions were further subdivided as: (a) centre, (b) periphery, (c) close, and (d) distant.

Energy dispersive X-ray spectroscopy was performed in a Quanta 200 environmental SEM (FEI Company, The Netherlands), operated at 20 kV accelerating voltage. Interfacial tissue approximately 5–10 μm from the implant surface at the centre and at the periphery of the porous network was analysed. As control, areas of the native trabecular bone (≥1.5 mm from the implant surface and unaffected by surgery) were also analysed. Two sample-pairs were used for the analysis. On each implant, EDX spectra were recorded at four different positions at the centre and the periphery of the porous network, and also in the native bone, considering only Al, Ti and V for Ti6Al4V, and Co, Cr, and Mo for CoCr specimens, in addition to Ca, P, O, C.

2.5. Osteocyte density and direct visualisation

Selected resin embedded bone-implant blocks were wet polished with 400–4000 grit SiC grinding paper. The samples were air-dried overnight prior to low-vacuum backscattered electron (BSE) SEM imaging in a Quanta 200 environmental SEM (FEI Company, The Netherlands) operated at 25 kV and 1 Torr water vapour pressure. The osteocyte density, i.e., the average number of osteocytes per mineralised surface (N.Ot/B.Ar), was quantified on BSE-SEM images recorded at ×200 magnification. All unmineralised areas in each recorded image were excluded by segmentation using ImageJ (imagej.nih.gov/ij) and the osteocytes were quantified using the Cell Counter plugin. Four sample-pairs were evaluated, and three separate observations were made at each region (centre, periphery, close, and distant).

For direct visualisation of osteocytes, the samples were sequentially immersed in 9% H_3PO_4 (for 30 s), rinsed in Milli-Q water (for 5 s), immersed in 5% NaOCl (for 5 min), rinsed again (for 30 s) and air-dried overnight. The samples were Au sputter-coated (~10 nm) for high vacuum secondary electron SEM imaging in an Ultra 55 FEG SEM (Leo Electron Microscopy Ltd, UK) operated at 20 kV [28].

2.6. Statistical analysis

The non-parametric Wilcoxon Signed Rank test for pair-wise analysis was used for histomorphometric analysis. In a site-matched manner (i.e., proximal vs. proximal, and distal vs. distal), the test (CoCr) implants in one femur were compared against the control (Ti6Al4V) implants in the contralateral femur, for each animal. No implants were excluded. The Kruskal-Wallis test followed by the Mann-Whitney *U* test were used for Raman spectroscopy, EDX, and osteocyte density analyses (SPSS Statistics, v.22, IBM Corporation); p values < 0.05 were considered statistically significant. Mean values ± standard deviations are presented.

3. Results

3.1. Implant geometry and surface characterisation

Both implant types, i.e., Ti6Al4V and CoCr had a similar design and overall appearance, with a solid top to facilitate insertion and primary fixation, and an integrated open-pore structure below.

Table 2
Morphometric data of the porous network of the implants characterised by micro-CT using a 3D analysis (n = 3).

	Ti6Al4V		CoCr	
	Mean	±SD	Mean	±SD
Material volume (%)	29.94	0.15	32.94	0.83
Porosity (%)	70.06	0.15	67.06	0.83
Surface area/volume ratio (mm^{-1})	11.41	0.03	12.23	0.18
Strut thickness (μm)	341.2	0.52	326.5	4.85
Strut separation (μm)	545.4	2.78	473.1	7.45

The quantitative measurements made by micro-CT showed minor differences between the implant materials in terms of porosity, surface area/volume ratio, strut thickness, and strut separation (Table 2). CoCr implants showed a rougher surface with more half molten particles at the surface yielding a higher surface area compared to Ti6Al4V, creating a slightly less defined pore structure with a smaller mean pore diameter (Fig. 3) and slightly lower total porosity. At higher magnification, however, the surface morphology appeared similar, with some micron and sub-micron structures resulting from flakes and protrusions.

The chemical composition of the implant surfaces was dominated by carbon and oxygen, apart from Ti, Al, and V for the Ti6Al4V implants and Co, Cr, and Mo for the CoCr implants (Table 3). Deconvolution of the carbon peaks showed that the contamination was predominantly found at 285.0 eV (>75%), indicating carbon bonds of the type C—C, C—H, and C=C, with some found at 286.5 eV (10%), indicating carbon with one bond to oxygen such as C—O and C—O—C, and minor signals at 288.1 eV and 288.9 eV indicating carbon with two bonds to oxygen and three bonds to oxygen, respectively.

The surface oxides on the Ti6Al4V implants were predominantly TiO_2, as indicated by the Ti 2p signal at 458 eV, while a minor Ti metal contribution was found at 454 eV. A minor amount of V was found at 516 eV indicating an oxidised state. The surface oxides on the CoCr implants were predominantly of Cr origin, with major Cr 2p signal at 576–580 eV, indicating oxide/oxohydroxide/hydroxide states with a minor contribution of Cr metal at 574 eV. A minor amount of Mo was found at 228–235 eV showing three peaks, indicating both metal and oxide contributions. The oxides and hydroxides were confirmed by the O 1s signal of all samples, found at 528–534 eV, with a shoulder towards higher binding energies, indicating a predominant oxide with some contributions of hydroxide.

3.2. Histology and histomorphometry

Both Ti6Al4V and CoCr constructs were well integrated in bone (Fig. 4) and no signs of inflammatory cells, fibrous encapsulation, or other adverse tissue reactions were detected. Mature trabecular bone was observed around the implants and extended into the porous network. The newly formed bone appeared to be in direct contact with the implant surface, filling the surface irregularities, and was also continuous with the existing trabecular bone of the femoral epiphysis. The formed bone made direct bone-implant contact at all vertical and horizontal levels of the constructs. Qualitatively, based on toluidine blue staining intensity, the bone formed inside the porous network exhibited a lower degree of maturity compared to the bone outside. However, the formed bone appeared morphologically similar to the surrounding native bone of the recipient site. This was characterised by the organised lamellar appearance of the trabeculae with numerous mature flattened osteocytes aligned parallel to the lamellar direction. At several locations, osteonal structures could be identified with concentric bone lamellae around central Haversian canals, particularly in close vicinity to the external surface of both Ti6Al4V and CoCr constructs. However, the presence of osteonal structures was not detected in the bone formed inside the porous network.

Both inside and outside the porous network, the spaces between the formed bone trabeculae were occupied by bone marrow, dominated by hematopoietic and adipose tissue. Furthermore, signs of ongoing bone remodelling were observed both external to the implant as well as inside the porous network, characterised by the appearance of areas of bone resorption concurrent with osteoblast seams depositing osteoid. In some of these remodelling sites osteoclasts could be identified. For both types of implants, several remodelling sites were found at the interface between the formed

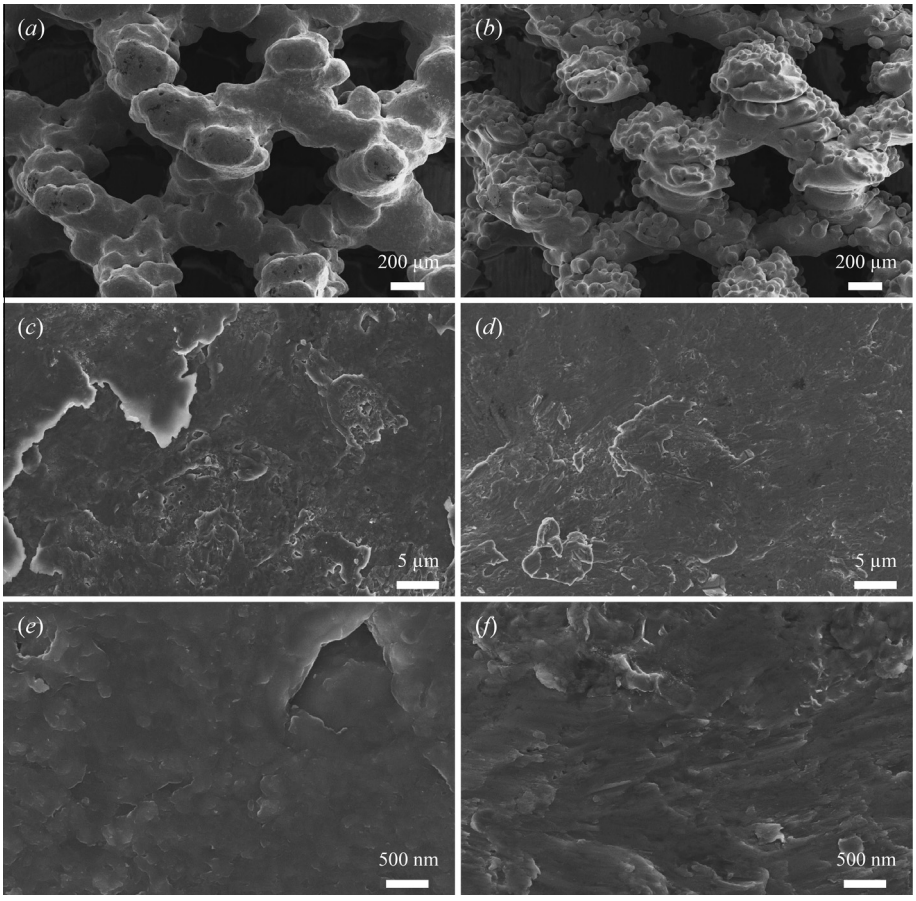

Fig. 3. Native implant surface. At low magnification, (a) Ti6Al4V shows a relatively smoother surface with less half-molten beads than (b) CoCr. At higher magnification, the surface topography of (c and e) Ti6Al4V and (d and f) CoCr appears similar at the micron and sub-micron scales.

Table 3
Relative surface composition (at.%) as measured by XPS ($n = 2$).

	Ti6Al4V		CoCr	
	Mean	±SD	Mean	±SD
Carbon (C)	40.4	1.98	46.7	0.28
Oxygen (O)	40.35	1.48	34.35	1.06
Titanium (Ti)	12.9	0.28	–	–
Aluminium (Al)	1.1	0.14	–	–
Vanadium (V)	0.5	0.00	–	–
Cobalt (Co)	0.4	0.00	4.95	0.78
Chromium (Cr)	–	–	10.9	0.14
Molybdenum (Mo)	–	–	0.6	0.00
Sodium (Na)	0.65*	0.35	0.05	0.07
Silicon (Si)	0.15	0.07	0.35	0.07
Zirconium (Zr)	0.1	0.00	0.02	0.02
Calcium (Ca)	0.4	0.00	–	–
Chlorine (Cl)	–	–	0.4	0.14
Manganese (Mn)	–	–	0.2	0.00
Iron (Fe)	1.75	0.64	–	–
Fluorine (F)	0.05	0.07	–	–

– signal at noise level in detail spectra (below 0.05–0.1 at.%).
* Amount of Na estimated, due to overlapping peaks at ~1070 eV for Na 1 s and Ti LMM Auger signals.

bone and the metal struts, thereby resulting in a lower degree of direct bone-implant contact at such locations (Fig. 5). Multinucleated giant cells were also detected, exclusively in association with the surface of both alloys, but not freely in the bone marrow. More multinucleated giant cells were observed at the top part of the porous network, i.e., between the lower side of the solid top and the upper struts. No metal debris or wear particulates were observed around or inside the porous network, for either Ti6Al4V or CoCr. While a few micron-sized metal spots were observed within the confines of the porous network, there was little biological response to such features as may be expected for isolated foreign particles. Therefore, they were considered to be either artefacts originating from sample preparation procedures (e.g., cutting and grinding) or otherwise metal that was still in continuity with the implant but only appearing as isolated fragments in 2D sections.

The bone area (BA) was similar for the two alloys, both inside and outside the porous network, while the total bone-implant contact (BIC) for Ti6Al4V was higher ($p < 0.01$) than CoCr. The BIC for Ti6Al4V was significantly higher than CoCr at both the centre ($p < 0.05$) and the periphery ($p < 0.01$) of the porous network, while no difference was observed at the solid top. No differences were observed in BA between Ti6Al4V and CoCr at any of the four locations. However, for both Ti6Al4V and CoCr, the highest BA was seen close/adjacent to the porous network, while the least BA was at the centre (Fig. 6).

3.3. Interfacial tissue composition

The composition of the interfacial tissue at the centre of the porous network, as well as the new bone adjacent to the implant appeared similar for Ti6Al4V and CoCr (Fig. 7a). The mineral phase was mainly carbonated apatite while other phosphate environments associated with early mineralisation were not detected. The organic phase consisted of collagen and commonly found amino acids proline (Pro), hydroxyproline (Hyp), phenylalanine (Phe), and tyrosine (Tyr). Phe and Tyr levels appeared to be higher

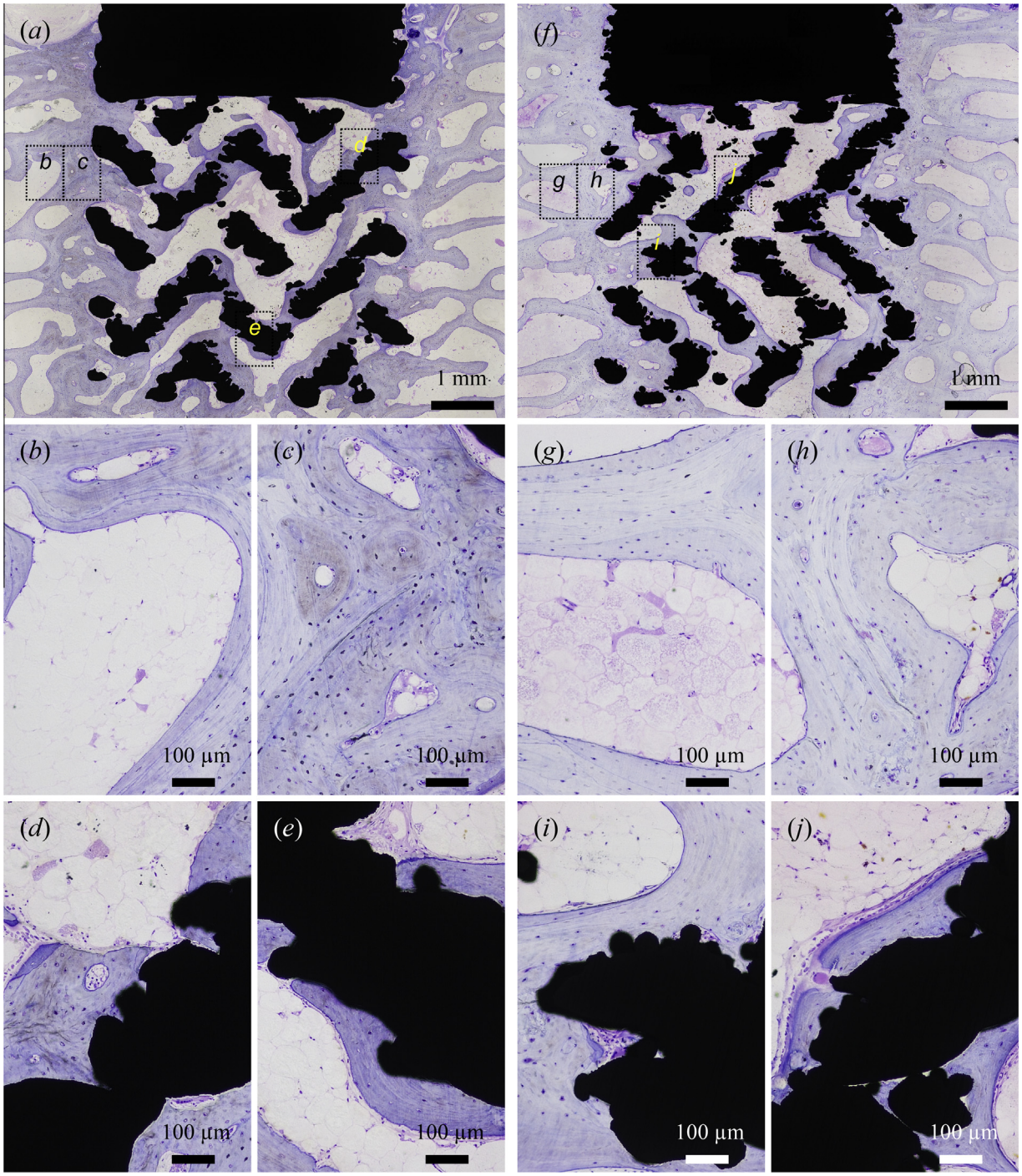

Fig. 4. Undecalcified toluidine blue stained sections of (a–e) Ti6Al4V and (f–j) CoCr implants. Overview images (a, f) show the pattern of bone formation around and inside the porous network. Higher magnification images of (b–e) Ti6Al4V and (g–j) CoCr correspond to the dotted boxes in (a) and (f).

at the interfacial tissue than outside the porous network, for both Ti6Al4V and CoCr. At each location (centre, periphery, and outside the porous network), although the mineral crystallinity was comparable for both materials (Fig. 7b), CoCr showed lower mineral crystallinity at the centre ($p < 0.03$) and the periphery ($p < 0.02$) of the porous network compared to the outside. For CoCr, the apatite-to-collagen ratio at the periphery of the porous network was lower ($p < 0.03$) than Ti6Al4V (Fig. 7c), which was also lower than at the centre of the porous network ($p < 0.01$) and outside ($p < 0.03$). The carbonate-to-phosphate ratio at the periphery of the porous network was higher for CoCr than Ti6Al4V ($p < 0.01$) (Fig. 7d), and was higher than at the centre of the porous network ($p < 0.03$).

The Ca/P ratio of the interfacial tissue (Ca/P = 1.4 ± 0.1 for all groups) was lower ($p < 0.02$ for all groups) than the native bone (Ca/P = 1.6 ± 0.2). However, the Ca/P ratio was comparable for CoCr and Ti6Al4V at the centre and the periphery of the porous network (Fig. 7e). Low levels of Cr, Co, and Ti were detected in the interfacial tissue; with only trace levels of Al, V, and Mo (Fig. 7f,g). However, due to the large volume from which characteristic X-rays are

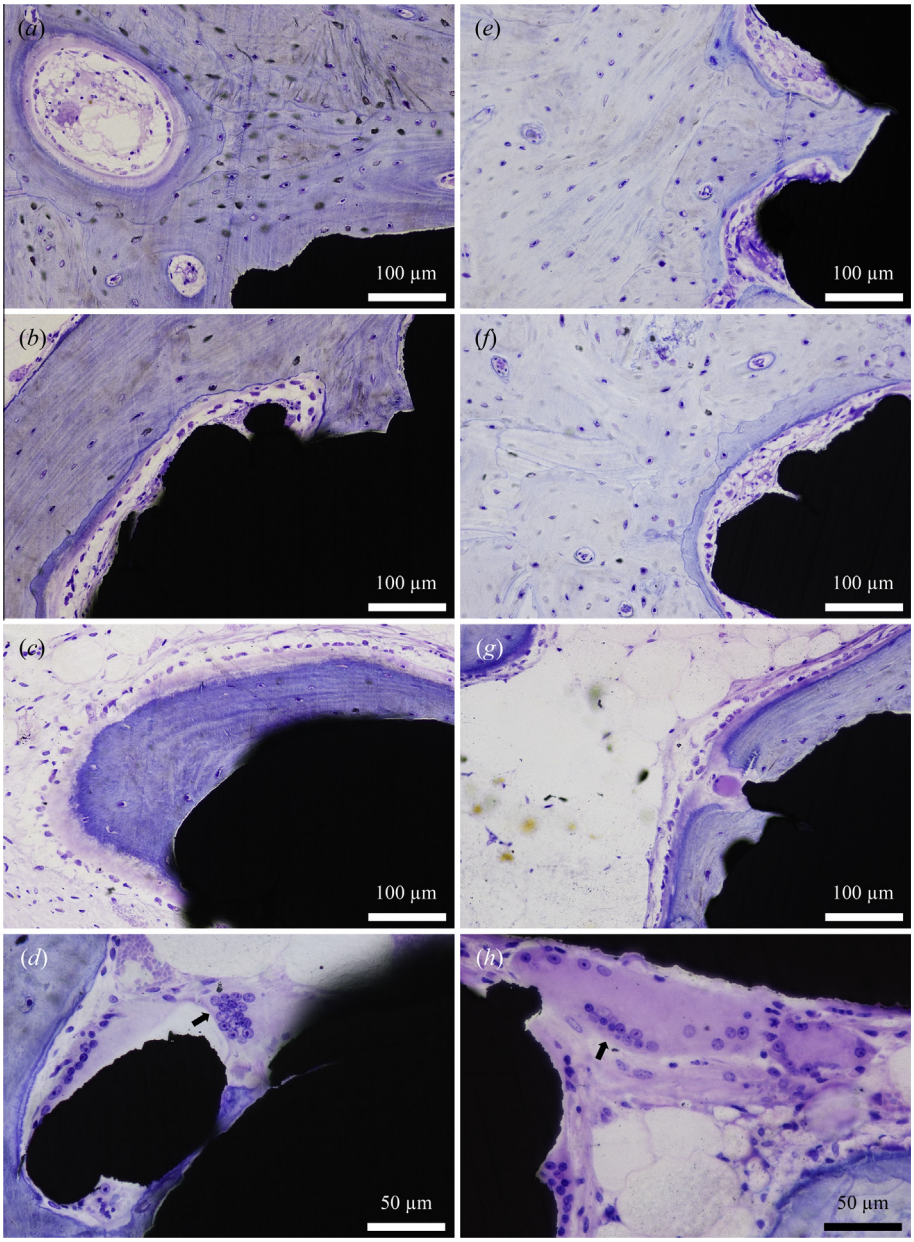

Fig. 5. Undecalcified toluidine blue stained sections of (a–d) Ti6Al4V and (e–h) CoCr implants. Remodelling sites as well as multinucleated giant cells (black arrows) were observed in association with the implant surface.

generated, the signal may be attributable to metal protrusions immediately under the bone surface, as well as metal smearing during sawing and grinding.

3.4. Direct visualisation of osteocyte morphology

On the polished bone-implant blocks, bone appeared well mineralised, with typical local variations in the *Z*- (atomic number) contrast corresponding to the extent of tissue mineralisation. Osteocyte lacunae appeared as elliptical, low contrast (dark) structures, which were aligned not only parallel to the lamellar direction, but also to the implant surface in areas of direct bone-implant contact (Fig. 8a,b). Larger low contrast structures within the mineralised matrix were identified as blood vessels, while those adjacent to the implant surface were resorption/remodelling sites. Osteocytes at (or near) the bone surface were generally aligned parallel to the receding marrow space. In areas of direct bone-implant contact, osteocytes were found to closely approach the Ti6Al4V (Fig. 8c) and CoCr surfaces (Fig. 8d), forming interconnected networks, and often making direct contact with the Ti6Al4V (Fig. 8e) as well as the CoCr implant surfaces (Fig. 8f) through cellular extensions, or dendrites, within canaliculi.

The overall osteocyte density (N.Ot/B.Ar) in the newly formed bone (inside and outside the porous network) was similar for Ti6Al4V (412 ± 31) and CoCr (417 ± 31). For Ti6Al4V, the N.Ot/B.Ar was comparable in the four regions analysed (centre, periphery, close, and distant). At the centre of the porous network, the N.Ot/B.Ar was comparable for the two alloys. On the contrary, the N.Ot/B.Ar at the periphery of the porous network was higher for CoCr ($p < 0.005$). For CoCr, the N.Ot/B.Ar increase at the periphery of the porous network appeared to be at the expense of osteocytes outside the porous network, as indicated by the significantly lower N.Ot/B.Ar at the close and distant regions than within the porous network ($p < 0.05$, and $p < 0.005$, respectively) (Fig. 8g–i).

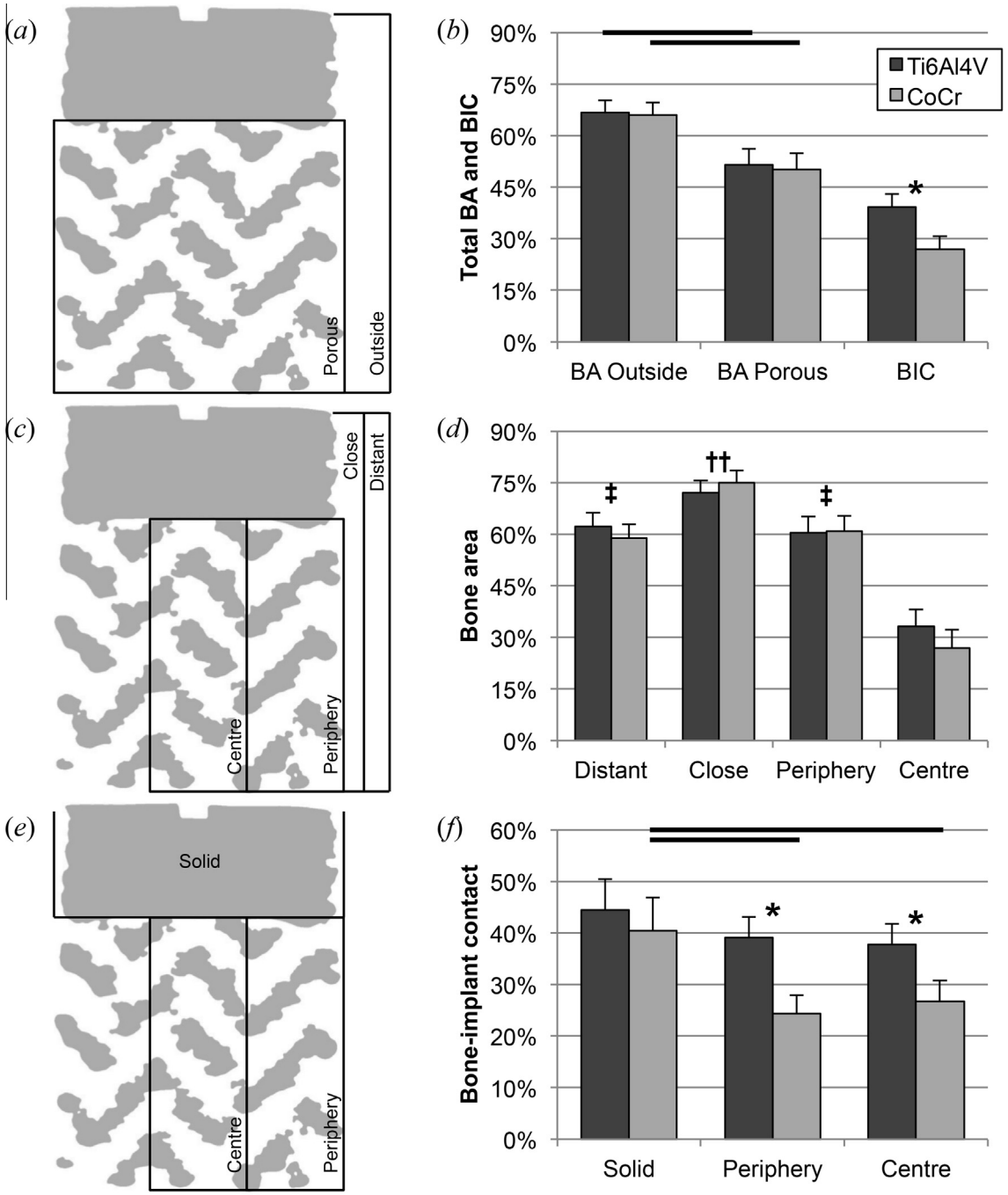

Fig. 6. (a and b) Overall histomorphometry (mean values ± SD, $n = 10$). Bone area (BA) measurements showed no differences between Ti6Al4V and CoCr, although higher amount of bone tissue was observed outside the porous network than inside. Bone-implant contact (BIC) measurements showed higher BIC for Ti6Al4V. (c and d) BA at the different locations analysed inside and around the implants. The highest BA was observed close to the implant. The least BA was observed in centre of the porous network. (e and f) BIC at the different locations analysed inside and around the implants. The BIC around the solid top was comparable for Ti6Al4V and CoCr. Inside the porous network, Ti6Al4V showed higher BIC than CoCr. The BIC for CoCr was higher around the solid top than inside the porous network. The illustrations (left) correspond to the quantitative analyses (right). (* = Statistical significance between Ti6Al4V and CoCr; Horizontal bars = Statistical significance between the groups indicated; †† = Significantly higher than all other locations; ‡ = Significantly higher than 'centre').

4. Discussion

This work demonstrates bone ingrowth into 3D printed CoCr implants having an open-pore architecture. Further, the results show that CoCr exhibits the potential to support osseointegration to the same extent as Ti6Al4V, after a relatively long-term healing phase. Whereas bone ingrowth has been referred to as bone formation within the irregularities and porosities on an implant surface [29], the concept of osseointegration revolves around new-formed bone enclosing an implant with perfect congruency to the implant form and surface irregularities, without any interpositioned connective tissue [30]. Although this description was later revised to include the resolution level, i.e., a direct contact between living bone and the implant – on the light microscopic level [31],

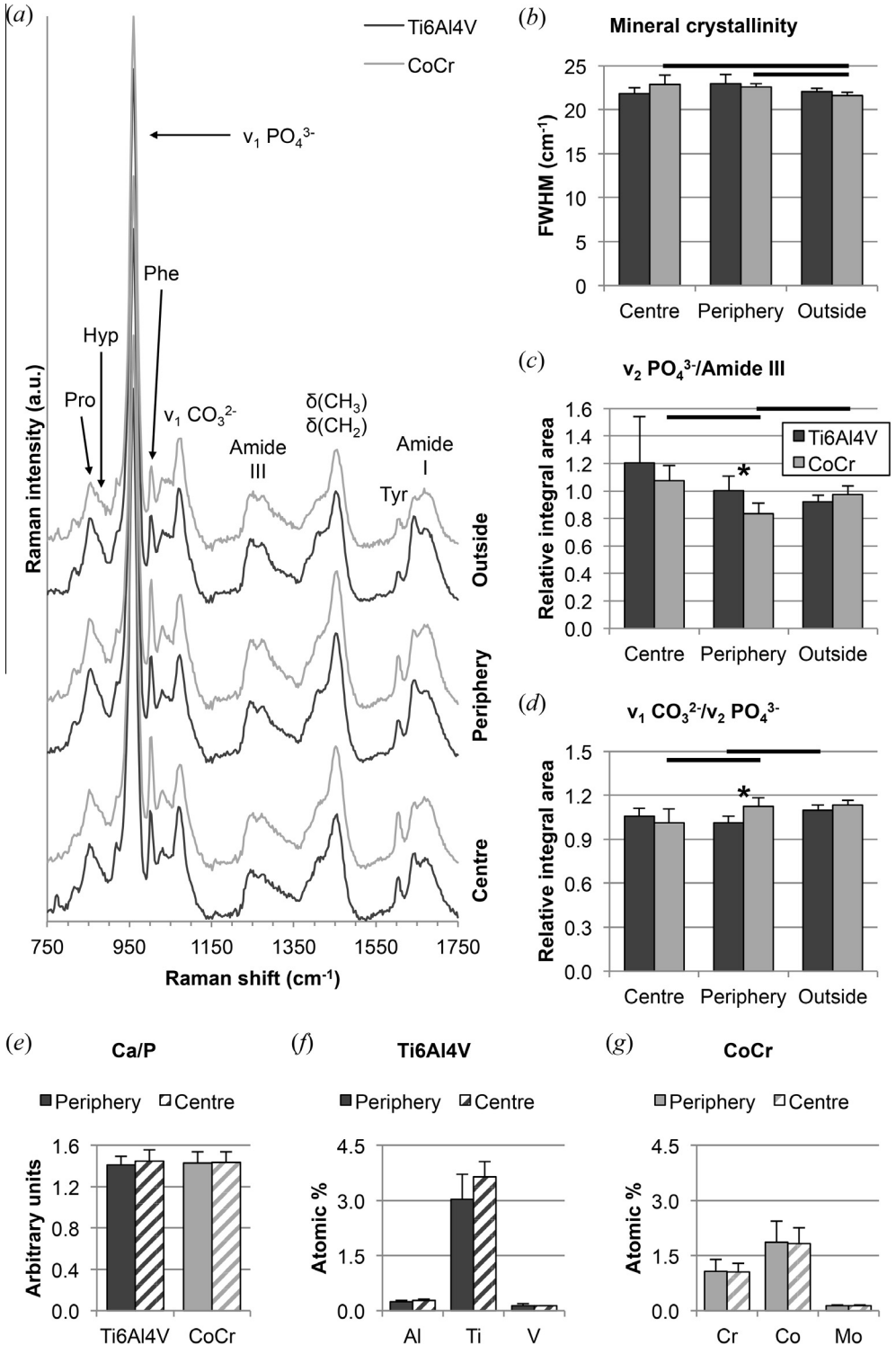

Fig. 7. (a) Raman spectra (average of spectra from five different locations) of the interfacial tissue at the centre and periphery of the porous network, and the newly formed bone outside (close and distant regions) the implants. (b–d) Raman metrics investigated for the interfacial tissue (mean values ± SD, * = Statistical significance between Ti6Al4V and CoCr; Horizontal bar = Statistical significance between the locations indicated, $n = 1$). (e–g) Elemental analysis by energy dispersive X-ray spectroscopy (EDX) of the interfacial tissue (mean values ± SD, $n = 2$).

no definition has yet been put forward for higher resolutions levels, or in terms of the composition, ultrastructure, or the overall biomechanical capacity of the interfacial tissue.

Correlative multiscale, structural analysis of the bone-implant interface [32] provides comprehensive information about the influence of an implant surface on the organisation of the micro- and nanoscale components of bone, e.g., bone apatite, collagen, and the osteocyte lacuno-canalicular network. Moreover, site-specific compositional analysis of the interfacial tissue, e.g., using Raman spectroscopy and energy dispersive X-ray spectroscopy, provides a novel dimension to the definition of osseointegration, i.e., assessment of quality rather than the quantity of new formed bone [20].

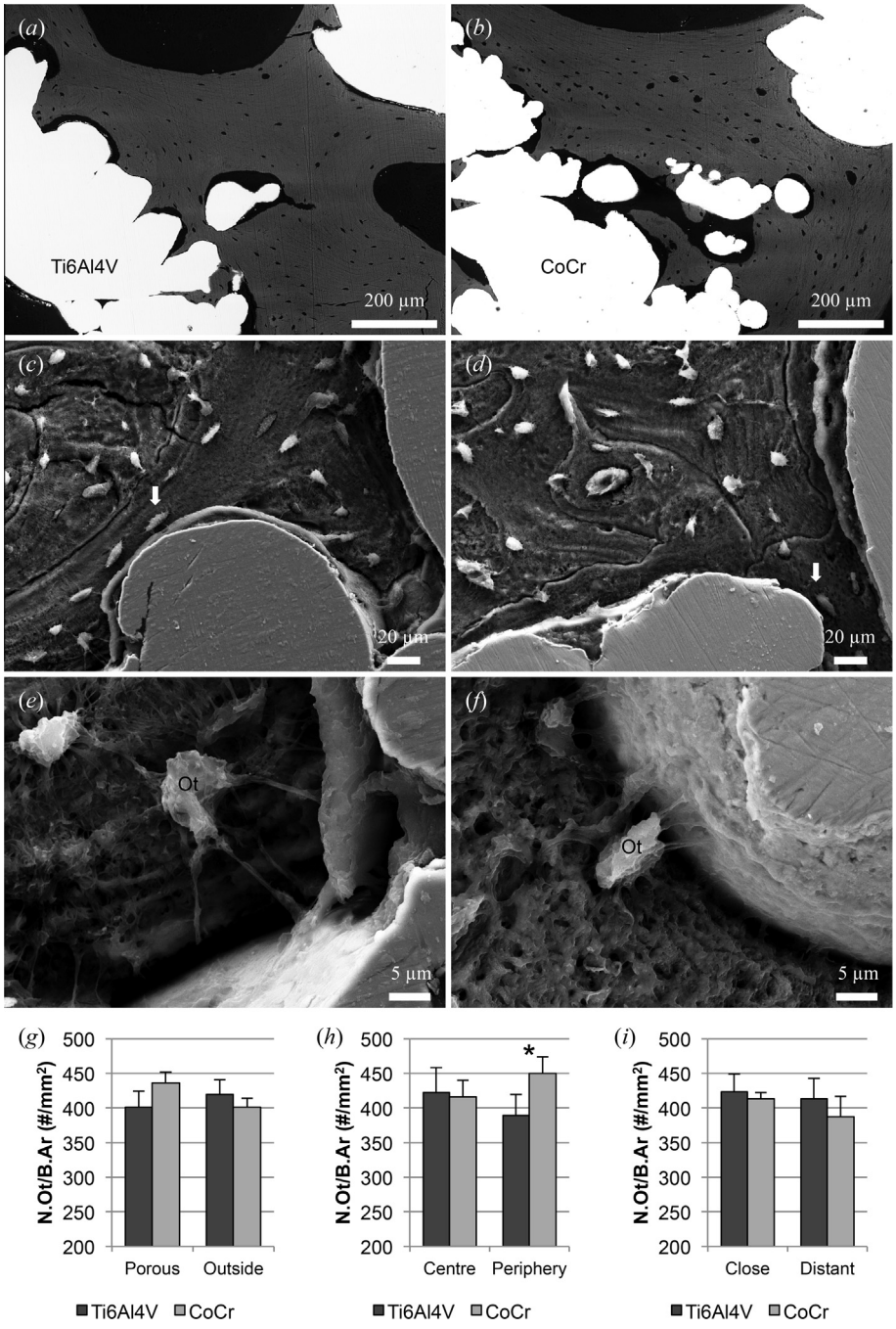

Fig. 8. Typical appearance of mineralised bone adjacent to the (a) Ti6Al4V and (b) CoCr implants. Osteocytes (Ot) in the interfacial tissue (white arrows) form interconnected networks adjacent to the (c) Ti6Al4V and (d) CoCr implant surfaces, and make direct contact with the (e) Ti6Al4V and (f) CoCr implant surfaces. (g–i) The average number of osteocytes within and outside the porous network (mean values ± SD, $n = 4$). * = Statistical significance between Ti6Al4V and CoCr.

The present results show that bone is regenerated in the innermost regions of the interconnected porous network for Ti6Al4V and CoCr, alike. The exact mechanism of bone formation within the confined interconnected porosity and the role of the physical and chemical properties of the implant surface are hitherto unknown. It is also not known whether bone formation occurred by progressive ingress from the margins of the recipient site or if the process also involved migration and subsequent differentiation of osteoprogenitor cells within the porous network. While neither scenario can be excluded, the latter is partially supported by the observation of ongoing remodelling in the centre of the porous network, indicating that the microenvironment established here provides biological cues for osteogenic differentiation and subsequent bone formation. In vitro experiments have shown that in contrast to solid implants, additively manufactured porous Ti6Al4V implant surface stimulates MC3T3-E1 osteoblast cell line functions, including cell attachment, proliferation, differentiation, and mineralisation [33]. Furthermore, porous Ti and Ti6Al4V implant surfaces support cell attachment and growth, without altering the expression of genes involved in osteogenic differentiation or affecting the alkaline phosphatase activity [34].

For the two alloys evaluated here, the average pore sizes of 470–545 µm and 67–70% porosity are in the range suggested to allow vascularisation and osteogenesis [35]. Pore sizes

(400–680 μm and 56–68% porosity) of porous Ti6Al4V scaffolds produced by 3D fibre deposition have been demonstrated to trigger higher bone formation than smaller ranges [36]. Furthermore, it has been shown that there is no threshold value for bone ingrowth into pore sizes ranging between 50 and 125 μm [37]. Indeed, in addition to bone ingrowth into the macroporosity, both CoCr and Ti6Al4V also support bone formation within surface irregularities and microporosities smaller than 100 μm.

With respect to the chemical composition, both Ti6Al4V and CoCr allowed similar amounts of bone formation, and hence comparable osseointegration. Although lower BIC was recorded within the porous network for CoCr (vs. Ti6Al4V), the lack of difference between the two materials in the solid region exempts the surface composition of CoCr from being exclusively responsible for the lower BIC values. Taken together, it appears that this combination of macro- and microporosity provides a suitable environment for bone regeneration, which is equally compatible with Ti6Al4V and CoCr as bulk materials.

Histology and BSE-SEM showed high amounts of organised lamellar bone inside the porous network, confirming that bone remodelling had occurred. Remodelling is a critical parameter for the long-term performance of bone-anchored implants where bone adjacent to the implant surface adapts in structure, amount, and composition in response to mechanical strain. The presence of osteocytes, aligned along lamellar directions, forming an interconnected network in close vicinity of the implant surface, and also directly contacting the implant surface through numerous dendritic extensions, particularly in the case of CoCr, attests to the presence of a functional load-sensing mechanism. Physiological loading of bone-anchored implants, in human, has been suggested to be important for continued osseointegration [32], possibly mediated via mechanical load sensing by osteocytes adjacent to the implant surface.

The BA was similar for the two alloys irrespective of the location, whether inside or outside the porous network. Moreover, the BIC recorded at the solid top region was also similar for both alloys. However, significantly lower BIC was observed for CoCr within the porous network (vs. outside, and vs. Ti6Al4V). And albeit not statistically significant, a trend towards slightly lower BIC inside the porous network than outside was also noted for Ti6Al4V. One explanation may be that the remodelling process is relatively slower adjacent to the CoCr surface than Ti6Al4V, since the non-contacting regions were primarily remodelling sites, and not fibrous tissue. The adaptive response of bone to dynamic loading, e.g., woven bone formation [38] and remodelling [39] are local processes. It is well known that interfacial stress transfer relies on various combinations of compressive, tensile, and shear stresses at different locations along the surface of orthopaedic implants [40]. It is plausible that under physiological loading, the biomechanical environment within the porous network is not the same as that outside. The extent of stress transfer into bone within the porous network may also not be similar for the two alloys, attributable to the difference in the overall stiffness of Ti6Al4V and CoCr constructs. The present investigation uses Ti6Al4V and CoCr implants of similar macro-geometry with only minor differences in terms of porosity and strut thickness. It has previously been shown that the stiffness of porous constructs is related to their relative density, and that the difference between the stiffness of Ti6Al4V and CoCr scales approximately by a factor of two – the stiffness of CoCr being twice that of Ti6Al4V [11]. Therefore, bone cells in the porous network may experience a higher degree of stress shielding inside the porous network than outside, and perhaps more adjacent to CoCr than Ti6Al4V, and therefore undergoes remodelling at different rates. The difference in the local biomechanical environment is supported by the observation of higher osteocyte density at the periphery of the porous network.

The CoCr alloy did not significantly alter the molecular structure or the elemental content of the mineralised interfacial tissue at long-term healing. The compositional parameters analysed using Raman spectroscopy, e.g., mineral crystallinity, the apatite-to-collagen ratio, and the carbonate-to-phosphate ratio were largely similar for both alloys, particularly at the centre of the porous network and in the new bone formed outside the implants. Therefore, in terms of the 'composite' nature of bone, the biomechanical characteristics of the mineralised tissue interfacing Ti6Al4V and CoCr may be considered to be similar. Being a marker of tissue age, the higher carbonate-to-phosphate ratio for CoCr (vs. Ti6Al4V) at the periphery of the porous network indicates 'more aged' tissue. This, in correlation with the higher osteocyte density observed in this region provides further evidence for slower bone remodelling in association with CoCr. Furthermore, a lower apatite-to-collagen ratio was observed for CoCr at the periphery of the porous network (vs. Ti6Al4V, and vs. centre and outside regions). It may be speculated that the change in the apatite-to-collagen ratio (i.e., relatively higher matrix content) could be a functional adaptation in response to the higher stiffness of CoCr. The Ca/P ratio of the interfacial tissue, determined by energy dispersive X-ray spectroscopy, was also similar for the two alloys. During bone formation, while initial (or primary) mineralisation of the organic matrix occurs relatively quickly to attain a high Ca/P ratio, the secondary mineralisation proceeds at a relatively slower rate [41]. This partly explains why the Ca/P ratio observed at implant surfaces is often lower than the native bone [20]. The lower Ca/P ratio of the interfacial tissue also corresponds with the lower degree of tissue maturation observed on histological evaluation.

Attributable to the particle sizes of the starting powders, the surface texture of Ti6Al4V and CoCr implants was different, with Ti6Al4V showing a slightly lower surface area/volume ratio (11.4 mm^{-1}) than CoCr (12.2 mm^{-1}). However, as the particle sizes are considerably larger than the size of cells and the atomisation process renders the surface extremely smooth, the surface texture is therefore not believed to significantly influence cellular response. It is nevertheless essential to highlight that ion release from the implant surface cannot be entirely excluded, and the cellular response to different ions cannot be easily predicted in vivo.

3D printing of CoCr by electron beam melting offers a key advantage in tailoring the construct design, e.g., the strut thickness, to lower the structural stiffness and match the elastic modulus of bone and therefore reduce stress shielding [42], as described by the Gibson & Ashby relationship [43]. The diamond shaped unit cell used here is isotropic. The mechanical and fatigue properties of anisotropic unit cells are considered to be dependent on the angle between the vertical struts of the unit cell and the loading direction [44]. The macrostructural symmetry in combination with microstructural isotropy resulting from the fabrication of the construct using atomised alloy powders implies that the construct may be able to endure multi-axial stresses better than solid implants machined from a cylinder of metal/alloy.

The limitations of this work must also be recognised, since the results are based on only one time-point (26 weeks), in non-loaded conditions. The clinical perspective, however, necessitates the demonstration of equivalent progress of osseointegration and mechanical stabilisation during early healing (e.g., 12 weeks), as well as maintenance of an organised hierarchical architecture at extended follow-up periods (e.g., 1–2 years), in functionally-loaded conditions. Due in part to the macro-geometry of the implants evaluated here, i.e., the interconnected open-pore architecture, and continuity of bone formed around and deep within the porous network of the implants, conventional biomechanical tests, e.g., removal torque, push-out, pull-out etc., may not be entirely reliable or applicable for such designs. Therefore, their ability to withstand functional loading must be interpreted largely

from the quantity and quality of bone formed within the porous network. However, morphometric assessment of osseointegration does not replace the demonstration of biomechanical stability of load-bearing implantable devices.

5. Conclusions

This work demonstrates, for the first time, the possibility to achieve bone ingrowth into open-pore CoCr constructs fabricated using electron beam melting, and attests to the potential for achieving osseointegration of bone-anchored CoCr implants with the possibility to customise the macro-geometry of the construct for clinical load-bearing applications. Ti6Al4V (39.2 ± 3.8%) showed higher total bone-implant contact (BIC) than CoCr (27 ± 3.7%). Nevertheless, bone formation patterns around and inside open-pore CoCr and Ti6Al4V implants were comparable, with a densification around the implant, and gradual ingrowth into the porous network, with more bone at the periphery than at the centre. Compared to Ti6Al4V, the CoCr alloy does not alter the composition of the mineralised interfacial tissue. Osteocytes make direct contact with the CoCr surface, with a higher osteocyte density in the periphery of the porous network adjacent to CoCr (vs. Ti6Al4V), perhaps attributable to differences in the local biomechanical environment due to the higher stiffness of CoCr.

Acknowledgements

The authors would like to thank Dr. Ezio Zanghellini at the Department of Applied Physics, Chalmers University of Technology for the kind assistance with Raman spectroscopy. This study was supported by the Swedish Research Council (grant K2015-52X-09495-28-4), the BIOMATCELL VINN Excellence Center of Biomaterials and Cell Therapy, the Region Västra Götaland, an ALF/LUA grant, the IngaBritt and Arne Lundberg Foundation, the Dr. Felix Neubergh Foundation, Promobilia, the Hjalmar Svensson Foundation, and the Materials Science Area of Advance at Chalmers and the Department of Biomaterials, University of Gothenburg.

References

[1] S. Tkachenko, O. Datskevich, L. Kulak, S. Jacobson, H. Engqvist, C. Persson, Wear and friction properties of experimental Ti-Si-Zr alloys for biomedical applications, J. Mech. Behav. Biomed. Mater. 39 (2014) 61–72.
[2] A.J. Saldivar-Garcia, H.F. Lopez, Microstructural effects on the wear resistance of wrought and as-cast Co-Cr-Mo-C implant alloys, J. Biomed. Mater. Res., Part A 74 (2005) 269–274.
[3] A. Chiba, K. Kumagai, N. Nomura, S. Miyakawa, Pin-on-disk wear behavior in a like-on-like configuration in a biological environment of high carbon cast and low carbon forged Co-29Cr-6Mo alloys, Acta Mater. 55 (2007) 1309–1318.
[4] N.G. Sotereanos, C.A. Engh, A.H. Glassman, G.E. Macalino, C.A. Engh Jr., Cementless femoral components should be made from cobalt chrome, Clin. Orthop. Relat. Res. 313 (1995) 146–153.
[5] C.A. Engh, J.D. Bobyn, A.H. Glassman, Porous-coated hip replacement. The factors governing bone ingrowth, stress shielding, and clinical results, J. Bone Joint Surg. Br. 69 (1987) 45–55.
[6] C.J. Sychterz, C.A. Engh, The influence of clinical factors on periprosthetic bone remodeling, Clin. Orthop. Relat. Res. 322 (1996) 285–292.
[7] J.D. Bobyn, A.H. Glassman, H. Goto, J.J. Krygier, J.E. Miller, C.E. Brooks, The effect of stem stiffness on femoral bone resorption after canine porous-coated total hip arthroplasty, Clin. Orthop. Relat. Res. 261 (1990) 196–213.
[8] R. Huiskes, H. Weinans, B. van Rietbergen, The relationship between stress shielding and bone resorption around total hip stems and the effects of flexible materials, Clin. Orthop. Relat. Res. 274 (1992) 124–134.
[9] P. Derand, L.E. Rannar, J.M. Hirsch, Imaging, virtual planning, design, and production of patient-specific implants and clinical validation in craniomaxillofacial surgery, Craniomaxillofac. Trauma Reconstr. 5 (2012) 137–144.
[10] L.E. Murr, S.M. Gaytan, E. Martinez, F. Medina, R.B. Wicker, Next generation orthopaedic implants by additive manufacturing using electron beam melting, Int. J. Biomater. 2012 (2012) 245727.
[11] L.E. Murr, K.N. Amato, S.J. Li, Y.X. Tian, X.Y. Cheng, S.M. Gaytan, et al., Microstructure and mechanical properties of open-cellular biomaterials prototypes for total knee replacement implants fabricated by electron beam melting, J. Mech. Behav. Biomed. Mater. 4 (2011) 1396–1411.
[12] T. Jinno, V.M. Goldberg, D. Davy, S. Stevenson, Osseointegration of surface-blasted implants made of titanium alloy and cobalt-chromium alloy in a rabbit intramedullary model, J. Biomed. Mater. Res. 42 (1998) 20–29.
[13] S.S. Jakobsen, J. Baas, T. Jakobsen, K. Soballe, Biomechanical implant fixation of CoCrMo coating inferior to titanium coating in a canine implant model, J. Biomed. Mater. Res., Part A 94 (2010) 180–186.
[14] A. Palmquist, T. Jarmar, L. Hermansson, L. Emanuelsson, A. Taylor, M. Taylor, et al., Calcium aluminate coated and uncoated free form fabricated CoCr implants: a comparative study in rabbit, J. Biomed. Mater. Res. B Appl. Biomater. 91B (2009) 122–127.
[15] K. Grandfield, A. Palmquist, S. Goncalves, A. Taylor, M. Taylor, L. Emanuelsson, et al., Free form fabricated features on CoCr implants with and without hydroxyapatite coating in vivo: a comparative study of bone contact and bone growth induction, J. Mater. Sci. - Mater. Med. 22 (2011) 899–906.
[16] L. Linder, Osseointegration of metallic implants. I. Light microscopy in the rabbit, Acta Orthop. Scand. 60 (1989) 129–134.
[17] L. Linder, K. Obrant, G. Boivin, Osseointegration of metallic implants. II. Transmission electron microscopy in the rabbit, Acta Orthop. Scand. 60 (1989) 135–139.
[18] P. Stenlund, S. Kurosu, Y. Koizumi, F. Suska, H. Matsumoto, A. Chiba, et al., Osseointegration enhancement by Zr doping of Co-Cr-Mo implants fabricated by electron beam melting, Addit. Manuf. 6 (2015) 6–15.
[19] A. Palmquist, A. Snis, L. Emanuelsson, M. Browne, P. Thomsen, Long-term biocompatibility and osseointegration of electron beam melted, free-form-fabricated solid and porous titanium alloy: experimental studies in sheep, J. Biomater. Appl. 27 (2013) 1003–1016.
[20] F.A. Shah, A. Snis, A. Matic, P. Thomsen, A. Palmquist, 3D printed Ti6Al4V implant surface promotes bone maturation and retains a higher density of less aged osteocytes at the bone-implant interface, Acta Biomater. 30 (2016) 357–367.
[21] K. Donath, G. Breuner, A method for the study of undecalcified bones and teeth with attached soft tissues. The Sage-Schliff (sawing and grinding) technique, J. Oral Pathol. 11 (1982) 318–326.
[22] V. Mazet, C. Carteret, D. Brie, J. Idier, B. Humbert, Background removal from spectra by designing and minimising a non-quadratic cost function, Chemometr. Intell. Lab. Syst. 76 (2005) 121–133.
[23] M.D. Morris, G.S. Mandair, Raman assessment of bone quality, Clin. Orthop. Relat. Res. 469 (2011) 2160–2169.
[24] M. Kazanci, H.D. Wagner, N.I. Manjubala, H.S. Gupta, E. Paschalis, P. Roschger, et al., Raman imaging of two orthogonal planes within cortical bone, Bone 41 (2007) 456–461.
[25] A. Roschger, S. Gamsjaeger, B. Hofstetter, A. Masic, S. Blouin, P. Messmer, et al., Relationship between the v(2)PO(4)/amide III ratio assessed by Raman spectroscopy and the calcium content measured by quantitative backscattered electron microscopy in healthy human osteonal bone, J. Biomed. Opt. 19 (2014) 065002.
[26] M. Kozielski, T. Buchwald, M. Szybowicz, Z. Blaszczak, A. Piotrowski, B. Ciesielczyk, Determination of composition and structure of spongy bone tissue in human head of femur by Raman spectral mapping, J. Mater. Sci. - Mater. Med. 22 (2011) 1653–1661.
[27] S. Gamsjaeger, A. Masic, P. Roschger, M. Kazanci, J.W. Dunlop, K. Klaushofer, et al., Cortical bone composition and orientation as a function of animal and tissue age in mice by Raman spectroscopy, Bone 47 (2010) 392–399.
[28] F.A. Shah, X. Wang, P. Thomsen, K. Grandfield, A. Palmquist, High-resolution visualization of the osteocyte lacuno-canalicular network juxtaposed to the surface of nanotextured titanium implants in human, ACS Biomater. Sci. Eng. 1 (2015) 305–313.
[29] H. Kienapfel, C. Sprey, A. Wilke, P. Griss, Implant fixation by bone ingrowth, J. Arthroplasty 14 (1999) 355–368.
[30] P.I. Brånemark, B.O. Hansson, R. Adell, U. Breine, J. Lindström, O. Hallen, et al., Osseointegrated implants in the treatment of the edentulous jaw. Experience from a 10-year period, Scand. J. Plast. Reconstr. Surg. Suppl. 16 (1977) 1–132.
[31] T. Albrektsson, P.I. Brånemark, H.A. Hansson, J. Lindström, Osseointegrated titanium implants. Requirements for ensuring a long-lasting, direct bone-to-implant anchorage in man, Acta Orthop. Scand. 52 (1981) 155–170.
[32] F.A. Shah, B. Nilson, R. Brånemark, P. Thomsen, A. Palmquist, The bone-implant interface – nanoscale analysis of clinically retrieved dental implants, Nanomed. Nanotechnol. Biol. Med. 10 (2014) 1729–1737.
[33] K.C. Nune, R.D. Misra, S.M. Gaytan, L.E. Murr, Interplay between cellular activity and three-dimensional scaffold-cell constructs with different foam structure processed by electron beam melting, J. Biomed. Mater. Res., Part A 103 (2015) 1677–1692.
[34] G.M. de Peppo, A. Palmquist, P. Borchardt, M. Lennerås, J. Hyllner, A. Snis, et al., Free-form-fabricated commercially pure Ti and Ti6Al4V porous scaffolds support the growth of human embryonic stem cell-derived mesodermal progenitors, ScientificWorldJournal 2012 (2012) 646417.
[35] V. Karageorgiou, D. Kaplan, Porosity of 3D biomaterial scaffolds and osteogenesis, Biomaterials 26 (2005) 5474–5491.
[36] J.P. Li, P. Habibovic, M. van den Doel, C.E. Wilson, J.R. de Wijn, C.A. van Blitterswijk, et al., Bone ingrowth in porous titanium implants produced by 3D fiber deposition, Biomaterials 28 (2007) 2810–2820.
[37] A.I. Itälä, H.O. Ylänen, C. Ekholm, K.H. Karlsson, H.T. Aro, Pore diameter of more than 100 microm is not requisite for bone ingrowth in rabbits, J. Biomed. Mater. Res. 58 (2001) 679–683.

[38] T. Sugiyama, J.S. Price, L.E. Lanyon, Functional adaptation to mechanical loading in both cortical and cancellous bone is controlled locally and is confined to the loaded bones, Bone 46 (2010) 314–321.
[39] P. Christen, K. Ito, R. Ellouz, S. Boutroy, E. Sornay-Rendu, R.D. Chapurlat, et al., Bone remodelling in humans is load-driven but not lazy, Nat. Commun. 5 (2014) 4855.
[40] R. Huiskes, The various stress patterns of press-fit, ingrown, and cemented femoral stems, Clin. Orthop. Relat. Res. 261 (1990) 27–38.
[41] E. Seeman, T.J. Martin, Co-administration of antiresorptive and anabolic agents: a missed opportunity, J. Bone Miner. Res. 30 (2015) 753–764.
[42] L.E. Murr, S.M. Gaytan, F. Medina, H. Lopez, E. Martinez, B.I. Machado, et al., Next-generation biomedical implants using additive manufacturing of complex, cellular and functional mesh arrays, Philos. Trans. R. Soc. London A: Math., Phys. Eng. Sci. 368 (2010) 1999–2032.
[43] L.J. Gibson, M.F. Ashby, Cellular Solids: Structure and Properties, Cambridge University Press, 1999.
[44] S. Amin Yavari, S.M. Ahmadi, R. Wauthle, B. Pouran, J. Schrooten, H. Weinans, et al., Relationship between unit cell type and porosity and the fatigue behavior of selective laser melted meta-biomaterials, J. Mech. Behav. Biomed. Mater. 43 (2015) 91–100.